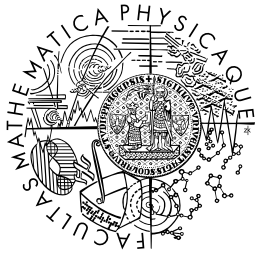

FACULTY
OF MATHEMATICS
AND PHYSICS
Charles University

BACHELOR THESIS

Jan Mareš

Thermal convection in an ice layer with a viscosity depending on the deformation history

Department of Geophysics

Supervisor of the bachelor thesis: prof. RNDr. Ondřej Čadek, CSc.

Study programme: Mathematical modelling

Study branch: Mathematics

Prague 2024

I declare that I carried out this bachelor thesis independently, and only with the cited sources, literature and other professional sources. It has not been used to obtain another or the same degree.

I understand that my work relates to the rights and obligations under the Act No. 121/2000 Sb., the Copyright Act, as amended, in particular the fact that the Charles University has the right to conclude a license agreement on the use of this work as a school work pursuant to Section 60 subsection 1 of the Copyright Act.

In ..... date ....

Author's signature

My deepest gratitude goes to Mgr. Martin Kihoulou, DiS. for his exceptional help with programming, code implementation and guidance throughout the development of this thesis. His kindness, patience and attitude were invaluable.

I also thank prof. RNDr. Ondřej Čadek, CSc. for assisting with the creation of the text, thesis structure and for giving me the opportunity to undertake this thesis. His support has been greatly appreciated.

Title: Thermal convection in an ice layer with a viscosity depending on the deformation history

Author: Jan Mareš

Department: Department of Geophysics

Supervisor: prof. RNDr. Ondřej Čadek, CSc., Department of Geophysics

Abstract: Thermal convection in the ice layer is a crucial process influencing the heat transfer, the internal structure of the icy shell and the potential habitability of icy moons in the outer Solar System. Despite the known significant impact of the grain size on thermal convection behaviour, only few models have integrated grain size evolution with realistic material parameters. In this study, we develop a numerical model to investigate the effect of grain size on thermal convection in the icy shells of these moons. Utilizing the finite-element method and a tracer method implemented in the FEniCS software, the model incorporates dynamically evolving grain size with realistic constitutive relations. Our findings indicate that the behaviour of our model closely mirrors those with constant grain size, suggesting that a constant grain size is a reasonable simplification. Regions with smaller grain sizes align with areas of higher stress, while elsewhere, the grain size reaches its maximum. This underscores the necessity of further research into the maximum grain size threshold.

Keywords: thermal convection, icy moons, finite elements, grain size evolution

Název: Termální konvekce v ledové vrstvě s viskozitou závislou na historii deformace

Autor: Jan Mareš

Katedra: Katedra geofyziky

Vedoucí práce: prof. RNDr. Ondřej Čadek, CSc., Katedra geofyziky

Abstrakt: Termální konvekce je klíčový proces ovlivňující přenos tepla, vnitřní strukturu ledové slupky a potenciální obyvatelnost ledových měsíců ve vnější sluneční soustavě. Přestože vliv velikosti zrn na chování termální konvekce je dobře znám, modely zahrnující vývoj velikosti zrna spolu s realistickými materiálnovými parametry jsou vzácné. V této práci představujeme numerický model, který zkoumá vliv vývoje velikosti zrn na tepelnou konvekci v ledových pláštích těchto měsíců. Model využívá metodu konečných prvků a metodu tracerů implementovanou v softwaru FEniCS a zahrnuje dynamicky se vyvíjející velikost zrn. Naše výsledky naznačují, že chování modelu se podobá modelům s konstantní velikostí zrn, což naznačuje, že předpoklad konstantní velikosti zrn je rozumným zjednodušením. Oblasti s menšími velikostmi zrn kopírují oblasti s vyšším napětím, zatímco jinde velikost zrna dosahuje svého maxima. To zdůrazňuje nutnost dalšího výzkumu maximální velikosti zrna v ledových slupkách měsíců.

Klíčová slova: termální konvekce, ledové měsíce, konečné prvky, vývoj velikosti zrna

Contents

Introduction

In recent decades, there has been a growing interest in studying icy objects in the outer Solar System. Missions such as Voyager, Galileo, and Cassini-Huygens have explored the systems of Jupiter and Saturn, revealing that some of their moons might possess large liquid subsurface oceans beneath their icy crusts [Nimmo and Pappalardo, 2016]. Other icy bodies, such as Neptune's moon Triton, visited by Voyager 2 in 1989 [Hansen et al., 2021], and the dwarf planet Ceres, explored by the Dawn mission [Ermakov et al., 2017], are also believed to have subsurface water reservoirs. Observations by the New Horizon spacecraft suggest that liquid water may exist inside Pluto despite its surface temperature being less than 45 K [Nimmo et al., 2016]. Notably, conditions in the oceans on Europa, Titan, and Enceladus, as indicated by the results from Galileo and Cassini-Huygens missions, could potentially support primitive life forms [Cockell et al., 2016]. These findings make these moons promising targets for future missions searching for life in the Solar System [Grasset et al., 2013, Lorenz et al., 2018, Howell and Pappalardo, 2020].

Realistic models of convective heat transfer in the ice shells of icy moons are still relatively rare. While current models usually account for the temperature dependence of viscosity, they often assume constant thermal properties, neglecting the effects of complex rheologies dependent on stress and grain size [Goldsby and Kohlstedt, 2001]. Whether heat transfer in the ice shell is dominated by conduction or convection is primarily determined by the grain size [Kihoulou et al., 2023]. However, the grain size on icy moons is a major unknown and may vary from 0.1 to 100 mm [Barr and McKinnon, 2007], leading to variations in viscosity spanning six orders of magnitude. Additionally, the grain size can change over time due to stress, temperature, and the presence of impurities (e.g., bubbles, dust particles, salts). Although several studies have described factors influencing grain size evolution [e.g., Journaux et al., 2019], it remains unclear how changes in grain size over time affect the heat transfer in the ice shell. This issue has only been addressed in a few studies that modelled ice flow with variable grain size but were simplified in other aspects [e.g., Barr and McKinnon, 2007].

In this thesis, we aim to investigate the role of grain size evolution in heat transfer on icy moons using a numerical model that incorporates realistic constitutive relations and the evolution of the grain size. Our goal is to provide the first estimate of the impact of grain size evolution on heat transfer in the outer shells of icy moons and to determine under which conditions the heat transfer is dominated by convection. To achieve this, we will develop a numerical code using the finite-element software FEniCS [Alnæs et al., 2015] and perform a series of simulations to show the effect of the grain size on the heat transfer for different model parameters.

1. Thermal convection in an ice layer

1.1 Governing equations

Thermal convection in an ice layer, particularly in the context of planetary bodies such as icy satellites, is a complex phenomenon that plays a crucial role in the thermal and mechanical evolution of these celestial objects. To gain a comprehensive understanding of this process, it is essential to formulate the problem mathematically by deriving the appropriate governing equations.

The fundamental equations governing thermal convection in an ice layer, expressed in the Boussinesq approximation [e.g., Kihoulou et al., 2023], are as follows:

$$\nabla \cdot \vec{v} = 0, \tag{1.1}$$

$$-\nabla p + \nabla \cdot \eta(\nabla \vec{v} + (\nabla \vec{v})^T) + \rho\, \vec{g} = \vec{0}, \tag{1.2}$$

$$\rho_0\, c_p \frac{\partial T}{\partial t} = \nabla \cdot (k \nabla T) - \rho_0\, c_p (\vec{v} \cdot \nabla T), \tag{1.3}$$

where $\vec{v}$ is the velocity, p is the pressure, T is the temperature, ρ is the density, η is the viscosity, c_p is the specific heat, k is the thermal conductivity, ρ_0 is the density at the reference temperature T_0 and $\vec{g}$ is the gravitational acceleration. The definitions of the constitutive relations for c_p, k, ρ and η are further described in section 1.3. We refer to equations (1.1), (1.2) and (1.3) as the continuity equation, the momentum equation and the energy equation, respectively. As in other studies, we assume that the ice is incompressible (1.1) and we neglect the effect of adiabatic and dissipative heating (1.3), which is likely to be of minor importance in icy moon applications (the dissipative number is $\sim 10^{-4} - 10^{-2}$).

1.2 Domain definition and boundary conditions

Equations (1.1)−(1.3) are solved in a 2-dimensional (2D) rectangular domain. The choice of the planar geometry is a meaningful way to approximate the ice shell of large icy moons, such as Europa, Titan or Ganymede, where the outer radius is bigger than 1500 km and the thickness of the ice layer is less than 100 km [Sotin et al., 2021]. In contrast, the assumption of the 2D geometry is a clear simplification and is only used to avoid the computational difficulties associated with 3D simulations. The computational domain, Ω, is illustrated in Figure 1.1.

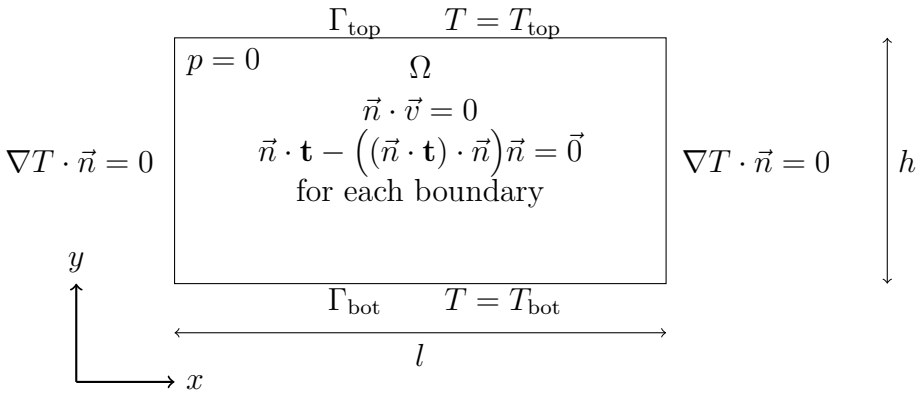

Figure 1.1: Description of the computational domain and boundary conditions

Symbol l denotes the length of the domain, h is the thickness of the ice layer and Γ_{bot} and Γ_{top} represent the bottom and top boundaries, respectively. The Cauchy stress tensor is denoted by $\mathbf{t}$ and $\vec{n}$ is the normal vector.

The domain is homogeneously heated from below and cooled from top, hence we prescribe the Dirichlet boundary conditions for the temperature on the top and bottom boundaries:

$$T = T_{\text{top}} \quad \text{on} \quad \Gamma_{\text{top}} \tag{1.4}$$

$$T = T_{\text{bot}} \quad \text{on} \quad \Gamma_{\text{bot}}. \tag{1.5}$$

Since the bottom boundary represents the phase interface between ice and water, temperature T_{bot} corresponds to the melting temperature of ice. Additionally, we assume isolating lateral boundaries. Hence, we prescribe the homogeneous Neumann boundary condition on both boundaries in the form

$$\nabla T \cdot \vec{n} = 0. \tag{1.6}$$

We assume that all boundaries are impermeable and free-slip. The first boundary condition for the momentum equation then reads

$$\vec{n} \cdot \mathbf{t} - \big((\vec{n} \cdot \mathbf{t}) \cdot \vec{n}\big)\vec{n} = \vec{0}, \tag{1.7}$$

and the boundary condition for the velocity takes the form

$$\vec{n} \cdot \vec{v} = 0. \tag{1.8}$$

Finally, we prescribe a condition for pressure by fixing $p = 0$ in the left top corner of the domain.

1.3 Material properties and constitutive relations

To accurately model the thermal convection in the ice shell, we need to account for the dependence of material parameters on the temperature. Thus, we

incorporate temperature-dependent constitutive relations for the thermal conductivity, specific heat and the density. We use the following relationship for the thermal conductivity in the form [Carnahan et al., 2021]:

$$k(T) = \frac{k_1}{T}. \tag{1.9}$$

Then, we use the relationship for the specific heat from McCord and Sotin [2005] in the form

$$c_p(T) = c_1 + c_2 T, \tag{1.10}$$

where k_1, c_1 and c_2 are constants listed in Table 1.1. Finally, we use the relationship for density adopted from Röttger et al. [1994] and Feistel and Wagner [2006]:

$$\rho(T) = \rho_0 \frac{a_0 + a_3 T_0^3 + a_4 T_0^4 + a_5 T_0^5 + a_6 T_0^6 + a_7 T_0^7}{a_0 + a_3 T^3 + a_4 T^4 + a_5 T^5 + a_6 T^6 + a_7 T^7}, \tag{1.11}$$

where ρ_0 is the density at the reference temperature T_0. All parameters are summarized in Table 1.1.

Symbol	**Physical quantity**	**Value**	**Unit**
h	height of the domain	100	km
l	length of the domain	200	km
g	gravitational acceleration	1.3	$\mathrm{m\,s^{-2}}$
k	thermal conductivity	2.1	$\mathrm{W\,m^{-1}\,K^{-1}}$
Q	activation energy	60	$\mathrm{kJ\ mol^{-1}}$
R	molar gas constant	8.314	$\mathrm{J\,K^{-1}\,mol^{-1}}$
T_{top}	top temperature	90	K
T_{bot}	bottom temperature	265	K
T_0	reference temperature	273	K
$\eta_{\text{cut-off}}$	cut-off viscosity	10^{24}	Pa s
ρ_0	density of ice at temperature T_0	917	$\mathrm{kg\,m^{-3}}$
a_0	density coefficient, eq. (1.11)	128.2147	Å
a_3	density coefficient, eq. (1.11)	-1.3152×10^{-6}	$\mathrm{Å\,K^{-3}}$
a_4	density coefficient, eq. (1.11)	2.4837×10^{-8}	$\mathrm{Å\,K^{-4}}$
a_5	density coefficient, eq. (1.11)	-1.6064×10^{-10}	$\mathrm{Å\,K^{-5}}$
a_6	density coefficient, eq. (1.11)	4.6097×10^{-13}	$\mathrm{Å\,K^{-6}}$
a_7	density coefficient, eq. (1.11)	-4.966×10^{-16}	$\mathrm{Å\,K^{-7}}$
c_1	constant specific heat coefficient, eq. (1.10)	185	$\mathrm{J\,kg^{-1}\,K^{-1}}$
c_2	linear specific heat coefficient, eq. (1.10)	7.037	$\mathrm{J\,kg^{-1}\,K^{-2}}$
k_1	thermal conductivity coefficient, eq. (1.9)	612	$\mathrm{W\,m^{-1}}$

Table 1.1: Physical parameters

While the definitions of the constitutive relations for ρ, c_p and k are relatively straightforward, the constitutive relation for the viscosity η is quite complex. According to Goldsby and Kohlstedt [2001], ice deformation is governed by four

primary creep mechanisms, which depend either only on the temperature (diffusion creep) or both on the temperature and stress (dislocation creep, grain boundary sliding and basal slip). Each creep mechanism is characterised by its specific viscosity.

Following Goldsby and Kohlstedt [2001], the viscosity for temperature- and stress-dependent mechanisms (dislocation creep, GBS, BS) is given by the following formula:

$$\eta(T, \dot{\varepsilon}_{II}) = \frac{1}{2} B^{\frac{-1}{n}} \dot{\varepsilon}_{II}^{\frac{1-n}{n}} d^{\frac{p}{n}} \exp\Big(\frac{Q}{nRT}\Big), \tag{1.12}$$

where B is the viscosity prefactor, n is the stress exponent, d is the grain size, p is the grain size exponent, Q is the activation energy for creep, R is the molar gas constant and T is the temperature. Finally, the second invariant of the strain rate tensor is defined

$$\dot{\varepsilon}_{II} = \sqrt{\frac{\dot{\boldsymbol{\varepsilon}} : \dot{\boldsymbol{\varepsilon}}}{2}}, \tag{1.13}$$

where $\dot{\boldsymbol{\varepsilon}}$ defined as

$$\dot{\boldsymbol{\varepsilon}} = \frac{1}{2}\Big(\nabla \vec{v} + (\nabla \vec{v})^T\Big). \tag{1.14}$$

Note that the values for the prefactor B differ from the values A listed in Goldsby and Kohlstedt [2001]. This is because we express the strain rate equation in terms of $\dot{\varepsilon}_{II}$, while the constitutive relations in Goldsby and Kohlstedt [2001] are formulated in terms of differential stress. The conversion formula yields [Durham and Stern, 2001]

$$B = \frac{1}{2} 3^{\frac{n+1}{2}} A. \tag{1.15}$$

Specific values for all parameters of each creep mechanism are listed in Table 1.2.

Creep Regime	A (MPa^{-n} s^{-1})	n	Q (kJ mol^{-1})
Dislocation creep ($T < 258$ K)	4.0×10^5	4.0	60
Dislocation creep ($T > 258$ K)	6.0×10^{28}	4.0	180
GBS ($T < 255$ K)	3.9×10^3	1.8	49
GBS ($T > 255$ K)	3.0×10^6	1.8	192
Basal slip	5.5×10^7	2.4	60

Table 1.2: Rheological parameters for stress-dependent creep mechanisms [Goldsby and Kohlstedt, 2001].

The viscosity given by the diffusion creep is determined by the relation

$$\eta(T) = \frac{2}{3} RTd^2 \frac{1}{84 V_m (D_v + \pi \delta D_b / d)}, \tag{1.16}$$

where V_m is a molar volume, D_v is the volume diffusion coefficient, δ is the grain boundary width and D_b is the grain boundary diffusion coefficient. In addition, D_v and D_b are determined as

$$D_b = D_{0,b} \exp\Big(-\frac{Q_b}{RT}\Big), \tag{1.17}$$

$$D_v = D_{0,v} \exp\Big(-\frac{Q_v}{RT}\Big), \tag{1.18}$$

where $D_{0,b}, D_{0,v}$ are constants listed in Table 1.3. The values of the remaining parameters are summarised in Table 1.3.

Symbol	**Description**	**Value**	**Unit**
V_m	Molar volume	1.97×10^{-5}	m^3
δ	Grain boundary width	9.04×10^{-10}	m
$D_{0,b}$	Preexponential, boundary diffusion	6.4×10^{-4}	$\mathrm{m}^2\mathrm{s}^{-1}$
$D_{0,v}$	Preexponential, volume diffusion	9.10×10^{-4}	$\mathrm{m}^2\mathrm{s}^{-1}$
Q_v	Activation energy, volume diffusion	59.4	kJ mol^{-1}
Q_b	Activation energy, boundary diffusion	49	kJ mol^{-1}

Table 1.3: Diffusion creep parameters [Goldsby and Kohlstedt, 2001].

The effective viscosity is then obtained by summing the reciprocals of the viscosities of all creep mechanisms [Goldsby and Kohlstedt, 2001]:

$$\frac{1}{\eta} = \frac{1}{\eta_{\text{diff}}} + \frac{1}{\eta_{\text{GBS}} + \eta_{\text{BS}}} + \frac{1}{\eta_{\text{disl}}}, \tag{1.19}$$

where η_{GBS}, η_{BS} and η_{disl} are viscosities given by (1.12) with corresponding parameters from the Table 1.2 and η_{diff} is obtained from (1.16). Finally, we limit the viscosity in the cold part of the domain by a maximal value $\eta_{\text{cut-off}}$ to reduce the viscosity contrast in the domain:

$$\eta_{\text{final}} = \min\{\eta, \eta_{\text{cut-off}}\}, \tag{1.20}$$

where we consider $\eta_{\text{cut-off}} = 10^{24}$ Pa s.

2. Numerical implementation

Having established the basic theoretical framework, we now turn our attention to the methodology employed in this study. With the governing equations that mathematically describe the behaviour of the system now obtained, we must proceed to solve them. For this purpose, we employ FEniCS, an open-source finite-element library designed for the numerical solution of partial differential equations [Alnæs et al., 2015, Logg et al., 2012].

2.1 Weak form of governing equations

The finite element method requires the governing equations to be in a weak form. This involves multiplying each equation by a test function and integrating over the domain while reducing the second-order spatial derivatives. First, we derive the weak form of the continuity equation (1.1) by multiplying it by a scalar test function χ and integrating over the domain Ω:

$$\int_\Omega \chi(\nabla \cdot \vec{v})\,\mathrm{d}V = 0. \tag{2.1}$$

Next, for the momentum equation (1.2), we multiply each term by a vector test function $\vec{w}$ and integrate over Ω. We obtain

$$\int_\Omega \vec{w} \cdot (-\nabla p + \nabla \cdot \eta\Big(\nabla\vec{v} + (\nabla\vec{v})^T\Big) + \rho\,\vec{g})\,\mathrm{d}V = 0. \tag{2.2}$$

Applying integration by parts to the pressure term, we get

$$\int_\Omega \vec{w} \cdot (-\nabla p)\,\mathrm{d}V = \int_\Omega (\nabla \cdot \vec{w}) p\,\mathrm{d}V - \int_{\partial\Omega} p(\vec{w} \cdot \vec{n})\,\mathrm{d}S. \tag{2.3}$$

As for the viscous term $\vec{w} \cdot \Big(\nabla \cdot \eta\Big(\nabla\vec{v} + (\nabla\vec{v})^T\Big)\Big)$, we proceed as follows

$$\begin{aligned}
\int_\Omega \vec{w} \cdot \Big(\nabla \cdot \eta(\nabla\vec{v} + \nabla^T\vec{v})\Big)\,\mathrm{d}V &= \int_\Omega \vec{w} \cdot (\nabla \cdot 2\eta\dot{\boldsymbol{\varepsilon}})\,\mathrm{d}V \\
&= \int_\Omega w_k\Big(2\eta\frac{\partial\dot{\varepsilon}_{k1}}{\partial x_1} + 2\eta\frac{\partial\dot{\varepsilon_{k2}}}{\partial x_2}\Big)\,\mathrm{d}V \\
&= -\int_{\partial\Omega} 2\eta w_k(\dot{\varepsilon}_{k1}n_1 + \dot{\varepsilon}_{k2}n_2)\,\mathrm{d}S \\
&\quad -\int_\Omega 2\eta\Big(\frac{\partial w_k}{\partial x_1}\dot{\varepsilon}_{k1} + \frac{\partial w_k}{\partial x_2}\dot{\varepsilon}_{k2}\Big)\,\mathrm{d}V \\
&= \int_{\partial\Omega} 2\eta\Big(\vec{w} \cdot (\dot{\boldsymbol{\varepsilon}} \cdot \vec{n})\Big)\,\mathrm{d}S - \int_\Omega 2\eta(\nabla\vec{w} : \dot{\boldsymbol{\varepsilon}})\,\mathrm{d}V \\
&= \int_{\partial\Omega} \vec{w} \cdot (\mathbf{t} \cdot \vec{n})\,\mathrm{d}S - \int_\Omega 2\eta\Big(\nabla\vec{w} : \mathrm{sym}(\nabla\vec{v})\Big)\,\mathrm{d}V,
\end{aligned} \tag{2.4}$$

where $\mathrm{sym}(\nabla\vec{v})$ denotes the symmetrical part of $\nabla\vec{v}$, defined as

$$\mathrm{sym}(\nabla\vec{v}) = \frac{1}{2}\Big(\nabla\vec{v} + (\nabla\vec{v})^T\Big). \tag{2.5}$$

Combining all the terms, the weak form of the momentum equation becomes

$$\int_\Omega (\nabla \cdot \vec{w})p - 2\eta\Big(\nabla\vec{w} : \mathrm{sym}(\nabla\vec{v})\Big) + \rho\,(\vec{g}\cdot\vec{w})\,\mathrm{d}V + \int_{\partial\Omega} -p(\vec{w}\cdot\vec{n}) + \vec{w}\cdot(\mathbf{t}\cdot\vec{n})\,\mathrm{d}S = 0. \tag{2.6}$$

Now we take into account the boundary conditions and further modify the equation. From the free-slip condition for velocity also follows the free-slip condition for the test function

$$\vec{v}\cdot\vec{n} = 0 \quad \Rightarrow \quad \vec{w}\cdot\vec{n} = 0. \tag{2.7}$$

This means that

$$\int_{\partial\Omega} -p(\vec{w}\cdot\vec{n})\,\mathrm{d}S = 0 \tag{2.8}$$

From the free-slip condition for $\mathbf{t}$, which is

$$\vec{n}\cdot\mathbf{t} - \Big((\vec{n}\cdot\mathbf{t})\cdot\vec{n}\Big)\vec{n} = \vec{0}, \tag{2.9}$$

we get

$$\int_{\partial\Omega} \vec{w}\cdot(\mathbf{t}\cdot\vec{n})\,\mathrm{d}S = 0 \tag{2.10}$$

Thus, the final weak form of the momentum equation is

$$\int_\Omega (\nabla\cdot\vec{w})p - 2\eta\Big(\nabla\vec{w} : \mathrm{sym}(\nabla v)\Big) - \rho\, g(\vec{e_y}\cdot\vec{w})\,\mathrm{d}V = 0. \tag{2.11}$$

Regarding the energy equation (1.3), we multiply it by a scalar test function τ and integrate over the domain Ω. This gives

$$\int_\Omega \tau\Big(\rho_0\, c_p \frac{\partial T}{\partial t}\Big) = \int_\Omega \tau\Big(\nabla\cdot(k\nabla T) - \rho_0\, c_p(\vec{v}\cdot\nabla T)\Big)\,\mathrm{d}V. \tag{2.12}$$

Next, we reduce the second-order derivative on the right-hand side

$$\begin{aligned}\int_\Omega \tau\Big(\nabla\cdot(k\nabla T)\Big)\,\mathrm{d}V &= \int_{\partial\Omega}\tau(k\nabla T\cdot\vec{n})\,\mathrm{d}S - \int_\Omega k(\nabla\tau\cdot\nabla T)\,\mathrm{d}V \\ &= -\int_\Omega k(\nabla\tau\cdot\nabla T)\,\mathrm{d}V + \int_{\partial\Omega}\tau(\vec{q}\cdot\vec{n})\,\mathrm{d}S.\end{aligned} \tag{2.13}$$

The heat flux through the boundary is zero from the boundary condition, which means that

$$\int_{\partial\Omega}\tau(\vec{q}\cdot\vec{n})\,\mathrm{d}S = 0. \tag{2.14}$$

The final form of the energy equation in the weak form is

$$\int_\Omega \rho_0\, c_p\frac{\partial T}{\partial t}\tau + k(\nabla\tau\cdot\nabla T) + \rho_0\, c_p(\vec{v}\cdot\nabla T)\tau\,\mathrm{d}V = 0. \tag{2.15}$$

Lastly, regarding our implementation, we use the Taylor-Hood element [Taylor and Hood, 1973], which is well-suited for solving incompressible flow problems. The Taylor-Hood element uses the polynomial of degree k for the velocity and the polynomial of degree $k-1$ for the pressure. We set $k = 2$. This method is pressure-robust. For the representation of the temperature, we choose a quadratic element.

2.2 Time derivative discretization and time step criterion

For the numerical solution of the equation (1.3), we employ the semi-implicit Crank-Nicholson scheme. This scheme replaces the time derivative with a finite difference approximation:

$$\frac{\partial T}{\partial t} = F \longrightarrow \frac{T - T_k}{\Delta t} = \frac{1}{2}(F + F_k), \tag{2.16}$$

where F refers to the term $k(\nabla\tau \cdot \nabla T) + \rho_0\, c_p(\vec{v} \cdot \nabla T)\tau$. The energy equation in its discretized form reads

$$\begin{aligned}\int_\Omega \rho_0\, c_p \frac{T - T_k}{\Delta t}\tau + \frac{1}{2}\Big[&\underbrace{\Big(k(\nabla\tau \cdot \nabla T) + \rho_0\, c_p(\vec{v} \cdot \nabla T)\tau\Big)}_{F} \\ &+ \underbrace{\Big(k(\nabla\tau \cdot \nabla T_k) + \rho_0\, c_p(\vec{v} \cdot \nabla T_k)\tau\Big)}_{F_k}\Big]\, \mathrm{d}V = 0.\end{aligned} \tag{2.17}$$

To regulate the length of the time step, we use the Courant–Friedrichs–Lewy (CFL) criterion in the form

$$\Delta t = \frac{1}{2}\min\left\{\frac{x_{\min}}{v_{\max}},\, x_{\min}^2 \frac{\rho c_p}{k}\right\}, \tag{2.18}$$

where $x_{\min}$ is the shortest element in the mesh and $v_{\max}$ is the highest velocity on the domain. The temperature-dependent quantities in equation (2.18) are evaluated at a constant temperature T_{mean} taken as the average of the top and bottom temperature boundary conditions.

2.3 Initial condition

To initialize the simulation, we need the initial condition for the temperature and velocity. The initial temperature is obtained by solving the stationary form of the energy equation (1.3), which is in the form

$$\nabla \cdot \Big(k(T)\nabla T\Big) = 0. \tag{2.19}$$

Since equation (2.19) is non-linear, we solve it iteratively, starting with linear profile

$$T = T_{\text{bot}} + \frac{T_{\text{top}} - T_{\text{bot}}}{h} y. \tag{2.20}$$

For details of the iterative method, see Algorithm 1.

Algorithm 1 Computational scheme of the conduction profile

$T_k \leftarrow$ linear temperature profile (2.20)
tempDifference $\leftarrow 0$
while tempDifference $> 10^{-3}$ **do**
  Solve Laplace problem (2.19)
  $T \leftarrow$ solution
  tempDifference $\leftarrow \dfrac{1}{h\,l}\displaystyle\int_\Omega \frac{|T_k - T|}{T}\,\mathrm{d}V$
  $T_k \leftarrow T$
end while

In addition, all ice creep regimes, except the diffusion creep are stress-dependent. As we do not know before the first time loop the stress and also the strain rate, we omit the effect of stress-dependent mechanisms in the first time step. Therefore, we use the diffusion creep to determine the viscosity of ice in the system and we use the temperature field obtained from Algorithm 1. Lastly, to facilitate the onset of convection, we prescribe a variation in the initial temperature profile in the form

$$T_{\text{init}} = T_{\text{alg}} + a\cos\Big(\frac{\pi x}{l}\Big)\sin\Big(\frac{\pi y}{h}\Big), \tag{2.21}$$

where T_{alg} is the temperature obtained from Algorithm 1 and a is the amplitude of the variation. In our case, we set $a = 0.05$ K.

2.4 Treatment of nonlinearities

During the simulation, we proceed through the main computational loop, where the Stokes problem (equations (1.1), (1.2)) and then the energy equation (equation (1.3)) are solved. The governing equations are due to the temperature-dependent parameters ρ, c_p, k and η nonlinear. The nonlinearity of the material parameters in the energy equation (1.3) is only weak, therefore we linearise it by evaluating them by the temperature from the previous time step. The momentum equation contains the term with viscosity depending not only on the temperature but also on the velocity as $\dot{\varepsilon}_{II}$ figures in the formula (1.12) for η. Simply using the velocity field from the previous time step would result in inaccuracies. Therefore, to obtain a sufficiently accurate solution, we use the Picard iterative algorithm [Picard, 1890], which is schematically illustrated in Algorithm 2.

Algorithm 2 Picard iterations of the Stokes problem

$\vec{v_k} \leftarrow$ solution of the Stokes problem
velDifference $\leftarrow 0$
while velDifference $> 10^{-3}$ **do**
  Solve the Stokes problem
  $\vec{v} \leftarrow$ solution
  velDifference $\leftarrow \dfrac{1}{h\,l}\displaystyle\int_\Omega \sqrt{\frac{(\vec{v} - \vec{v_k})\cdot(\vec{v} - \vec{v_k})}{\vec{v}\cdot\vec{v}}}\,\mathrm{d}V$
  $\vec{v_k} \leftarrow \vec{v}$
  if iterations > 10 **then**
    break
  end if
end while

The number of Picard iterations is either restricted by the difference of solutions between two iterations or by the upper limit of 10 iterations. The whole computational scheme is illustrated in Algorithm 3.

Algorithm 3 Computational scheme

Define mesh, function spaces, functions on mesh, equations, boundary conditions, initial conditions
Define endtime
time $\leftarrow 0$
$T_k \leftarrow$ linear temperature profile (2.20)
tempDifference $\leftarrow 0$
while tempDifference $> 10^{-3}$ **do**
  Solve Laplace problem (2.19)
  $T \leftarrow$ solution
  tempDifference $\leftarrow \dfrac{1}{h\,l}\displaystyle\int_\Omega \frac{|T_k - T|}{T}\,\mathrm{d}V$
  $T_k \leftarrow T$
end while
Add temperature variation
$\vec{v_k} \leftarrow$ solution of Stokes problem from the diffusion creep
while time $\leq$ endtime **do**
  velDifference $\leftarrow 0$
  while velDifference $> 10^{-3}$ **do**
    Solve the Stokes problem
    $\vec{v} \leftarrow$ solution
    velDifference $\leftarrow \dfrac{1}{h\,l}\displaystyle\int_\Omega \sqrt{\frac{(\vec{v} - \vec{v_k}) \cdot (\vec{v} - \vec{v_k})}{\vec{v} \cdot \vec{v}}}\,\mathrm{d}V$
    $\vec{v_k} \leftarrow \vec{v}$
    if iterations > 10 **then**
      break
    end if
  end while
  Update Δt from CFL criterion
  Solve Energy equation
  $T_k \leftarrow$ solution
  time $\leftarrow$ time + Δt
end while

3. Program testing

3.1 Thermal convection benchmark

In chapter 1, we have established the required relationships to begin simulating the thermal convection. In this chapter, we create a model of thermal convection with simple rheology. This model is compared to the thermal convection benchmark [Blankenbach et al., 1989] using two parameters which we introduce later. For the benchmark, unlike in chapter 1, we consider constant material properties and we further assume that the density in the momentum equation (1.2) is given by the linear relationship

$$\rho = \rho_0\Big(1 - \alpha(T - T_0)\Big), \tag{3.1}$$

where ρ_0 is the density at the reference temperature T_0 and α is the thermal expansion coefficient. Here, for a moment, we do not omit the term $\rho_0 \dfrac{d\vec{v}}{dt}$ on the right side of the momentum equation (1.2).

Let us introduce the following non-dimensional parameters:

$$\vec{x} = D\vec{x}', \qquad t = \frac{D^2}{\kappa}t', \qquad \vec{v} = \frac{\kappa}{D}\vec{v}', \qquad p = \rho_0\, gDp', \qquad T = T_{top} + \Delta T T', \tag{3.2}$$

where D is the characteristic dimension, in our case, the height of the domain h, and g is the magnitude of the gravitational acceleration; the thermal diffusivity κ, kinematic viscosity ν and ΔT are defined as follows:

$$\kappa = \frac{k}{\rho_0\, c_p}, \qquad \nu = \frac{\eta}{\rho_0}, \qquad \Delta T = T_{\text{bot}} - T_{\text{top}}. \tag{3.3}$$

Then the governing equations after incorporating the dimensionless parameters become

$$\nabla' \cdot \vec{v}' = 0, \tag{3.4}$$

$$-\nabla' p' + \nabla' \cdot \eta'(\nabla'\vec{v}' + (\nabla'\vec{v}')^T) + Ra(T' - T_0')\vec{e}_z = \frac{1}{Pr}\frac{d\vec{v}'}{dt'}, \tag{3.5}$$

$$\frac{\partial T}{\partial t} = -\vec{v}' \cdot \nabla' T' + \Delta' T', \tag{3.6}$$

where Ra and Pr,

$$Ra = \frac{\rho_0 \alpha \Delta T D^3 g}{\eta\kappa}, \qquad Pr = \frac{\nu}{\kappa}, \tag{3.7}$$

denote the Rayleigh and the Prandtl numbers, respectively.

In the case of thermal convection in the ice shell of icy moons, the Prandtl number can be estimated from below as

$$Pr = \frac{\nu}{\kappa} = \frac{\eta c_p}{k} \geq 2.5 \times 10^{19}, \tag{3.8}$$

where we have computed the quantities of the material properties in (3.8) for T_{bot}. Therefore, the whole term $\frac{1}{Pr}\frac{d\vec{v}'}{dt'}$ can be neglected.

For the benchmark, we use the non-dimensional equations (3.4) − (3.6). We compare our results with those published by Blankenbach et al. [1989] for three different Rayleigh numbers:

1a) $Ra = 10^4$

1b) $Ra = 10^5$

1c) $Ra = 10^6$

Now, let us introduce the parameters, which rate the properties of a convecting system. The Nusselt number is a non-dimensional parameter, which is defined as the ratio of a convective to a conductive (total) heat flux through the top boundary:

$$Nu = \frac{q_{\text{conv}}}{q_{\text{cond}}}. \tag{3.9}$$

The next value, which we are going to compare with the benchmark, is the root mean square velocity, defined as

$$v_{rms} = \frac{1}{h\,l}\sqrt{\int_\Omega \vec{v}\cdot\vec{v}\,dV}. \tag{3.10}$$

In each numerical simulation, we wait for the convection to reach a steady state and then we compare the statistical properties defined above with the values from Blankenbach et al. [1989].

3.2 Domain definition and boundary conditions

We perform the benchmark test in a box with an aspect ratio of 1. The bottom temperature is set to 1 and the top temperature is set to 0 as illustrated in Figure 3.1. All other boundary conditions remain the same as in Figure 1.1.

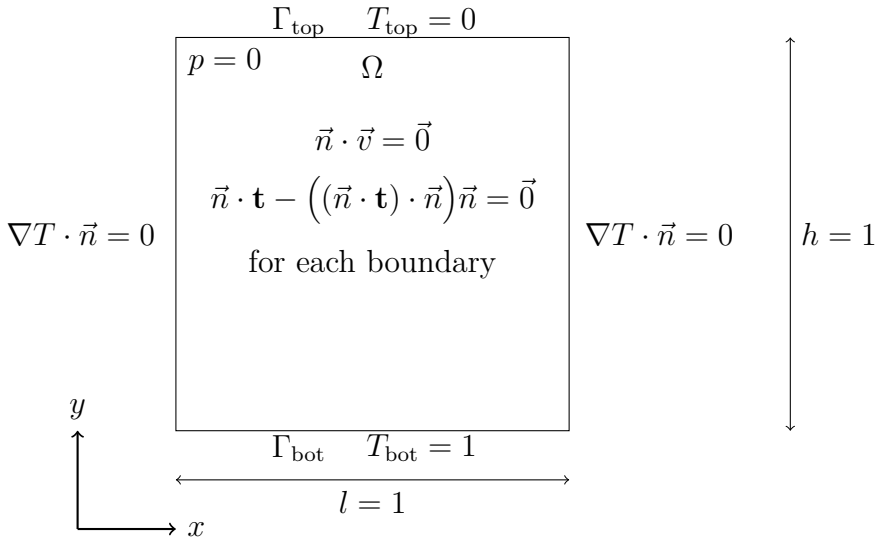

Figure 3.1: Convection benchmark domain description

The resolution of the box is chosen 50×50 cells for Cases 1a) and 1b), and 100×100 cells for Case 1c).

3.3 Convection benchmark results

The steady states obtained for the three considered cases, are shown in Figures 3.2 – 3.4 for each Case 1a) – 1c), where the black contours illustrate the isotherms. The corresponding table comparing our results with those of Blankenbach et al. [1989] together with relative errors are shown in Table 3.1. The evolutions of Nu and v_{rms} for all studied cases are shown in Figure 3.5.

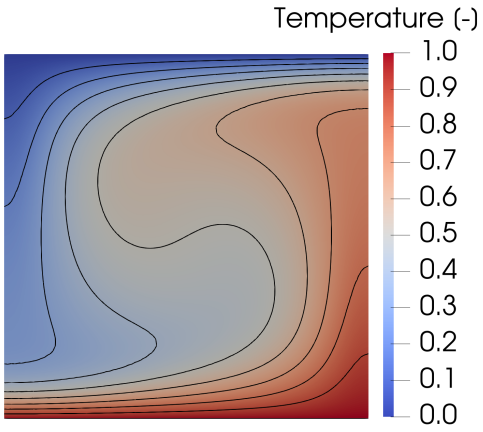

Figure 3.2: Steady state, $Ra = 10^4$

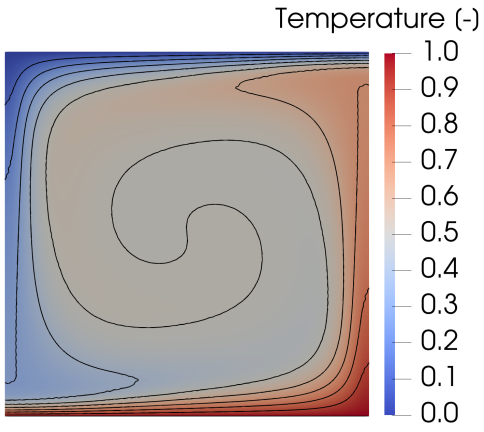

Figure 3.3: Steady state, $Ra = 10^5$

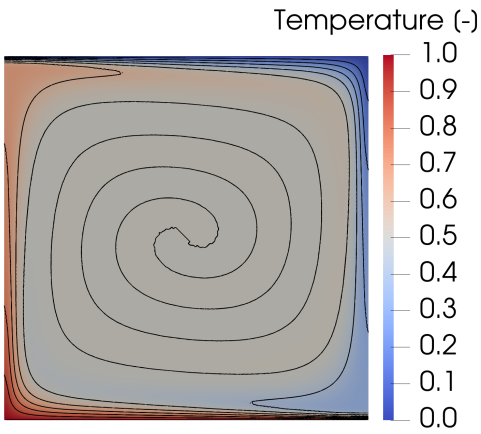

Figure 3.4: Steady state, $Ra = 10^6$

	Blankenbach et al. [1989]	This study	Relative error
(1a)			
Nu	4.884	4.895	0.225%
v_{rms}	42.865	42.851	0.033%
(1b)			
Nu	10.534	10.625	0.863%
v_{rms}	193.215	193.214	0.0005%
(1c)			
Nu	21.972	22.207	1.069%
v_{rms}	834.990	833.438	0.186%

Table 3.1: Comparison of our results with those of Blankenbach et al. [1989]

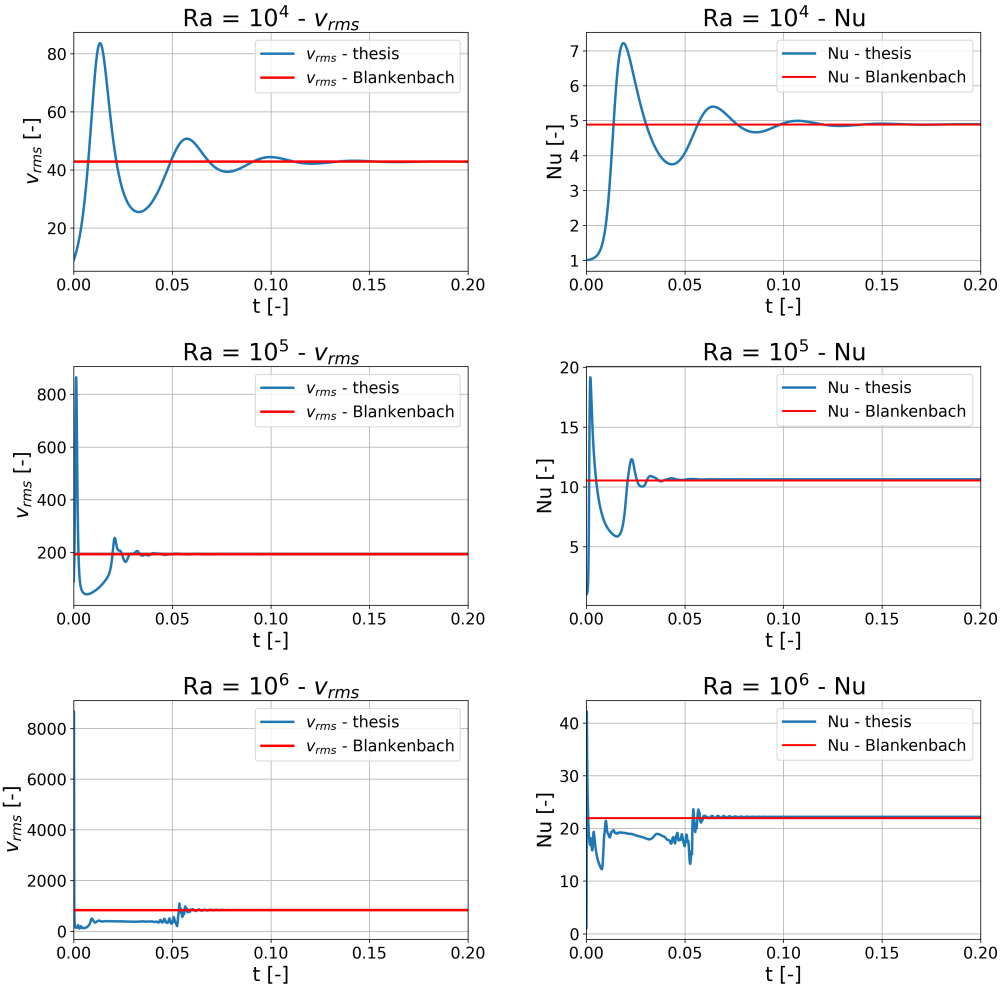

Figure 3.5: Comparisons of Nu and v_{rms} for the three cases considered in the convection benchmark. The values obtained by Blankenbach et al. [1989] are shown by the red lines.

The convection in Figures 3.2 – 3.4 takes place over the whole domain and reaches a steady state in each case. We have verified that our values for Nu and

v_{rms} match the values from Blankenbach et al. [1989] with satisfactory precision, indicating that we can proceed with simulating thermal convection in the ice layer using realistic physical parameters. Hence, we will again consider the dimensional form of the governing equations.

4. Thermal convection with a constant grain size

Before turning our attention to the problem of evolving grain size, we will develop a model of thermal convection with the rheology described in chapter 1, but we will assume that the grain size is constant in space and time. We are faced with the question of choosing the grain size. To explore the influence the grain size has on the behaviour of the convecting system, we perform numerical simulations for three different values of the grain size. The grain sizes are chosen such that the viscosity given by the diffusion creep at the bottom boundary is equal to

2a) $\eta_0 = 10^{14}$ Pa s

2b) $\eta_0 = 10^{15}$ Pa s

2c) $\eta_0 = 10^{16}$ Pa s

The grain size is derived from the diffusion creep formula (1.16) which can be transformed to the form

$$RTd^3 - \frac{2}{3}\,84dD_v\eta_0 V_m - \frac{2}{3}\,84\pi\delta D_b\eta_0 V_m = 0. \tag{4.1}$$

Solving this equation for each η_0 in Cases 2a), 2b) and 2c), we obtain the following grain sizes:

2a) $d = 0.45$ mm

2b) $d = 1.42$ mm

2c) $d = 4.48$ mm

The evolution of the system for each grain size is simulated over a time period of 100 million years. The final states are compared in Figures 4.1, 4.2 and 4.3 for Cases 2a), 2b) and 2c), respectively.

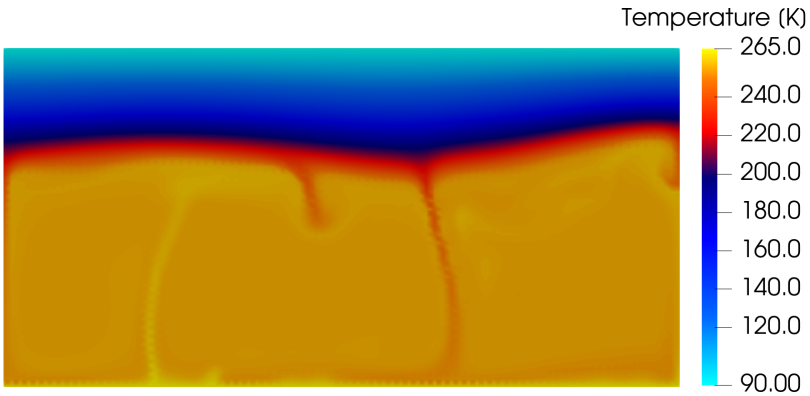

Figure 4.1: Case 2a)

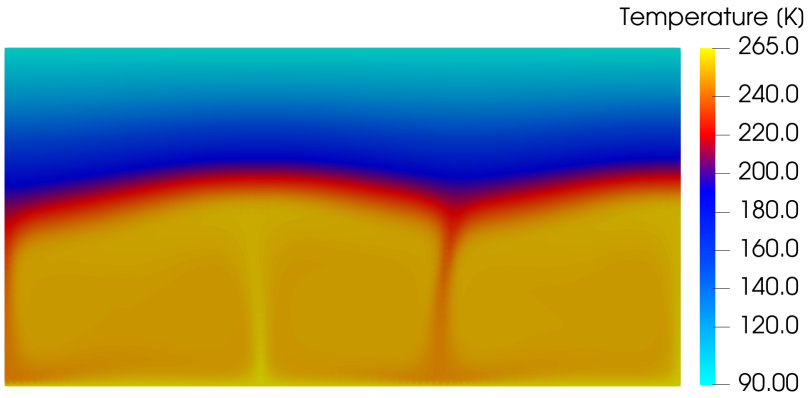

Figure 4.2: Case 2b)

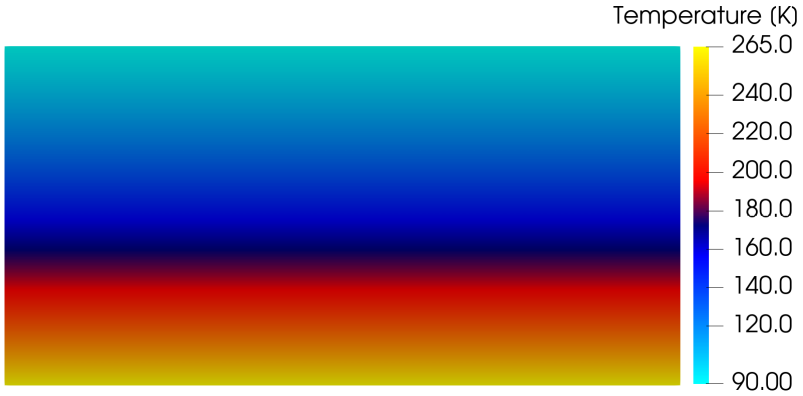

Figure 4.3: Case 2c)

Inspection of the figures suggests that the convection in the ice shell with the realistic rheology with constant grain size occurs only for the grain sizes 0.45 mm and 1.42 mm, whereas the system enters a conductive mode for the grain size 4.48 mm. Thus, the critical value of the grain size which determines, whether the system is in the convective or the conductive regime lies between 1.42 mm and 4.48 mm. The vigour of the convection is significant for Case 2a), which we can observe in Figure 4.1. The system acts chaotically and the Nusselt number takes on the value 2.863. On the other hand, Figure (4.2) illustrates the creation of two convective cells for Case 2b) and the Nusselt number acquires the value 1.984. Finally, the system in Case 2c) is fully in the conductive regime and no convection occurs.

5. Grain size evolution

In this chapter, we develop a model where we dynamically adjust the grain size throughout the simulation. This novel approach to modelling thermal convection incorporates the evolution of the grain size with realistic rheology. Several studies describing the grain size evolution have been published to this date [e.g., Behn et al., 2021, Linow et al., 2012, Wang et al., 2024]. Our model is based on the findings of Behn et al. [2021], who suggests that grain size growth is driven by the Arrhenius-type relationship stated below, while the grain size reduction is influenced by dislocation creep and grain boundary sliding (GBS) creep. The parameters describing the grain size evolution were derived from the investigation of the laboratory and ice core data obtained from the GRIP (Greenland Ice Core Project) measuring.

5.1 Consititutive relations

According to Behn et al. [2021], the grain size evolution is given by the formula in the form

$$\dot{d} = \dot{d}_{gg} - \dot{d}_{red}, \tag{5.1}$$

where $\dot{d}$ is the rate of the grain size change, $\dot{d}_{gg}$ is the rate of the grain growth and $\dot{d}_{red}$ is the rate of the grain size reduction. The formula for $\dot{d}_{gg}$ is given by the Arrhenius-type relationship

$$\dot{d}_{gg} = p_{gg}^{-1} d^{1-p_{gg}} K_{gg} \exp\Big(-\frac{Q_{gg}}{RT}\Big), \tag{5.2}$$

where p_{gg} is the grain growth exponent, K_{gg} is the grain growth constant and Q_{gg} is the activation energy for the grain growth; specific values for these constants are listed in Table 5.1. The Arrhenius dependence indicates, that the fastest growth rate is expected for high temperatures at the interface of the ice shell and the subsurface ocean, whereas the smallest growth of the grain is likely to occur in the colder areas on the surface. The formula for the grain size reduction is determined as

$$\dot{d}_{red} = \frac{(\lambda_{\mathrm{GBS}} - \beta\lambda_{\mathrm{GBS}} + \beta\lambda_{\mathrm{disl}})d^2}{c\gamma}\sigma_{II}\dot{\varepsilon}_{II}, \tag{5.3}$$

where c, γ, λ_{GBS}, λ_{disl} are constants described in Table 5.1 and β can be expressed as

$$\beta = \frac{\dot{\varepsilon}_{II,\mathrm{disl}}}{\dot{\varepsilon}_{II,\mathrm{GBS}} + \dot{\varepsilon}_{II,\mathrm{disl}}}. \tag{5.4}$$

Additionally, the values for λ_{disl} and λ_{GBS} are uncertain and are not determined independently [Behn et al., 2021], thus we further assume that $\lambda_{\mathrm{disl}} = \lambda_{\mathrm{GBS}}$. Hence, for simplicity, let us denote $\lambda = \lambda_{\mathrm{disl}} = \lambda_{\mathrm{GBS}}$.

Symbol	Description	Value	Unit
Q_{gg}	Activation energy for grain growth	42	kJ mol^{-1}
K_{gg}	Grain growth rate constant (lab)	1.36×10^{-20}	m$^{7.1}$ s^{-1}
K_{gg}	Grain growth rate constant (lab+ice core)	9.15×10^{-18}	m$^{6.03}$ s^{-1}
p_{gg}	Grain growth exponent (lab)	7.1	-
p_{gg}	Grain growth exponent (lab+ice core)	6.03	-
γ	Average specific grain boundary energy	0.065	J m^{-2}
λ	Fraction of work done by dislocation and GBS creep to change grain boundary area	0.005–0.05	-
c	Geometric constant	3	-

Table 5.1: Grain size evolution parameters [Behn et al., 2021].

5.2 Numerical implementation

The equations (5.2) and (5.3) describe changes in the size of individual ice grains, which are advected with the flow. We have to treat the information about the grain size as a material property of ice and advect it with the flow. For this purpose, we utilize a tracer method developed by Kihoulou [2024]. Advection of Lagrangian tracers is a numerical method for solving the transport part of the partial differential equations, representing the advected quantity by a finite number of infinitesimal points. Each tracer holds information about its position and size.

In the beginning, tracers are regularly distributed within each cell of the mesh with a given number of tracers inside the cell. Tracers are advected using the obtained velocity field through the second-order Runge-Kutta method:

$$\begin{aligned} \vec{v}_1 &= \vec{v}^{\,i-1}(\vec{r}^{\,i-1}), \\ \vec{v}_2 &= \vec{v}^{\,i-1/2}\left(\vec{r}^{\,i-1} + \frac{\Delta t}{2}\vec{v}_1\right), \\ \vec{r}^{\,i} &= \vec{r}^{\,i-1} + \Delta t \vec{v}_2, \end{aligned} \tag{5.5}$$

where $\vec{r}$ is the position vector. Throughout the simulation, the number of tracers in each cell is monitored, and when it falls below a minimum threshold, additional tracers are introduced to prevent the occurrence of empty cells. The grain size within each cell is determined by the arithmetic mean of the grain sizes of the tracers within that cell. This averaged grain size is then used in our rheological relationships for viscosity (1.12) and (1.16). Subsequently, the grain size of each tracer is updated using the equations (5.2) and (5.3).

Moreover, we limit the grain size from above with the value $d_{\max} = 1.5$ mm, so as not to dampen the convection. This step is justified by the presence of impurities (bubbles, dust, ions and microparticles) in ice which prevent further growth. Conversely, we allow the grain size to decrease even when it reaches the maximum size $d_{\max}$. The grain size evolution process is outlined in Algorithm 4. We choose $d = 1.5\,\text{mm}$ as the initial grain size on the whole mesh. The modified version of the computational scheme is illustrated in Algorithm 5.

Algorithm 4 Grain size evolution scheme

$d_{\text{old}} = d$
$d_{\text{growth}} = \min\left\{d_{\max},\ d_{\text{old}} + \dot{d}_{gg} \cdot \Delta t\right\}$
$d_{\text{new}} = d_{\text{growth}} - \dot{d}_{red} \cdot \Delta t$
$d = d_{\text{new}}$

Algorithm 5 Computation scheme

Define mesh, function spaces, functions on mesh, equations, boundary conditions, initial conditions
Introduce tracers on the mesh and set the initial grain size
Define endtime
time $\leftarrow 0$
$T_k \leftarrow$ linear temperature profile (2.20)
tempDifference $\leftarrow 0$
while tempDifference $> 10^{-3}$ **do**
  Solve Laplace problem (2.19)
  $T \leftarrow$ solution
  tempDifference $\leftarrow \dfrac{1}{h\,l}\displaystyle\int_\Omega \frac{|T_k - T|}{T}\,\mathrm{d}V$
  $T_k \leftarrow T$
end while
Add temperature variation
$\vec{v_k} \leftarrow$ solution of the Stokes problem from the diffusion creep
while time $\leq$ endtime **do**
  Add tracers to cells
  velDifference $\leftarrow 0$
  while velDifference $> 10^{-3}$ **do**
    Solve the Stokes problem
    $\vec{v} \leftarrow$ solution
    velDifference $\leftarrow \dfrac{1}{h\,l}\displaystyle\int_\Omega \sqrt{\frac{(\vec{v} - \vec{v_k}) \cdot (\vec{v} - \vec{v_k})}{\vec{v} \cdot \vec{v}}}\,\mathrm{d}V$
    $\vec{v_k} \leftarrow \vec{v}$
    if iterations > 10 **then**
      break
    end if
  end while
  Update Δt from CFL criterion
  Solve Energy equation
  $T_k \leftarrow$ solution
  Update grain size of each tracer with Algorithm 4
  Advect tracers
  Interpolate grain size on the mesh using the tracers
  time $\leftarrow$ time + Δt
end while

5.3 Verification of tracer advection module

Before performing the simulations of the thermal convection with grain size evolution, we test the correctness of the advection of tracers by performing a benchmark test specified in Fullsack [1995]. We prescribe a vortex velocity field and let the tracers advect during the simulation. In the beginning, we label each tracer with a value reflecting its starting position and then compare the label of the nearest tracer with an analytical solution of the vortex flow.

The angular velocity is prescribed analytically as

$$\omega(r) = \omega_0 \frac{r}{r_0} \exp\left(-\frac{r}{r_0}\right), \tag{5.6}$$

where $r = \sqrt{x^2 + y^2}$ is the radial distance from the origin, $\omega_0 = 0.3$ and $r_0 = 0.25$. In the beginning, we regularly distribute 60×60 tracers into a $[-0.3, 0.3] \times [-0.3, 0.3]$ square. We assign each tracer with the scalar quantity $F(x, y, t)$ defined for each tracer as

$$F(x, y, 0) = x. \tag{5.7}$$

The tracers are advected by the velocity field (5.6) using the second-order Runge-Kutta method. Here, we choose a constant time step $\Delta t = 1$. Then, we compare the analytical solution for the evolution of F, given by

$$F(x, y, t) = x\cos(\omega(r)t) + y\sin(\omega(r)t) \tag{5.8}$$

with the quantity of F of the nearest tracer at coordinates:

- $(r = 0.2r_0, 0)$
- $(r = 0.4r_0, 0)$
- $(r = 0.6r_0, 0)$

The results which we obtain for each point are shown in Figure 5.1.

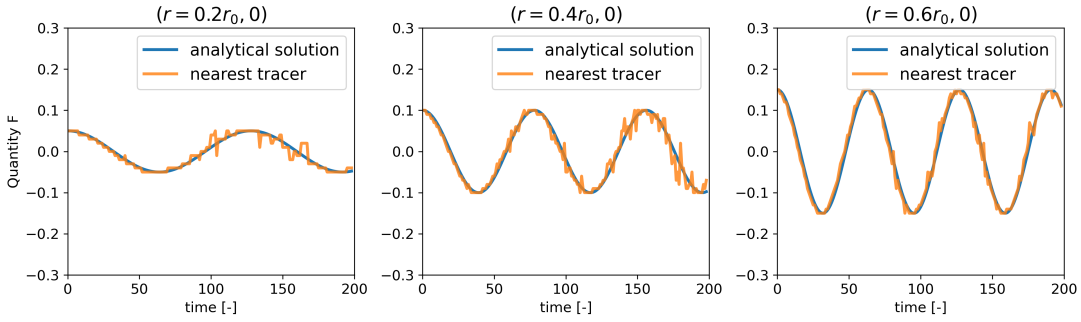

Figure 5.1: Comparison of analytical solution with the quantity of F of the nearest tracer

The simulations were performed on the mesh with a resolution of 50×50 cells. The results show that the analytical solution matches the quantity F of the nearest tracer with sufficient precision at each point and inaccuracies occur because of interpolating to the nearest tracer. However, both numerical and analytical solutions have the same amplitude and frequency, which confirms that the advection is implemented correctly and we can proceed to simulate the convection in the ice shell with evolving grain size.

5.4 Results

We now get to the core of this study as we perform the simulations of thermal convection in the icy shell with evolving grain size. Based on the parameters from Behn et al. [2021], two sets of values exist for parameters in Table 5.1 - lab and lab+ice core obtained either from the laboratory (lab) or from the GRIP project (lab+ice core). The values of λ vary from 0.005 to 0.05. Hence, we perform a simulation combining each set of parameters (lab, lab+ice core) with the limit values of λ. This gives us 4 options:

4a) lab, $\lambda = 0.005$

4b) lab, $\lambda = 0.05$

4c) lab + ice core, $\lambda = 0.005$

4d) lab + ice core, $\lambda = 0.05$

The snapshots of temperature fields and grain sizes from the simulations of each case are shown in Figures 5.2 – 5.5. Each snapshot was taken at a different time because we chose a state where two convective cells are visible and the convection is more stable. It is then clear where the grains change their sizes.

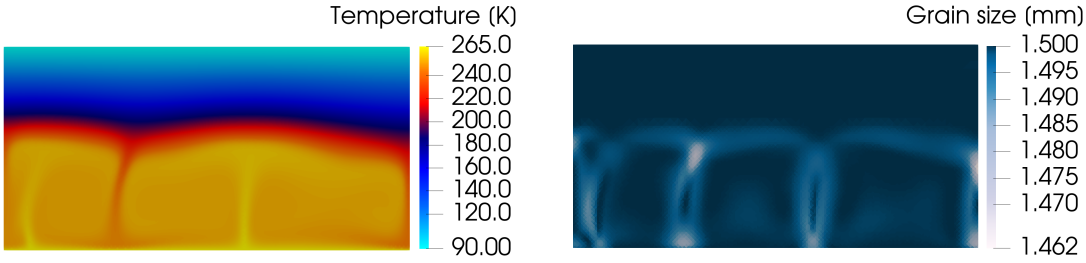

Figure 5.2: Case 4a), 96 Myr

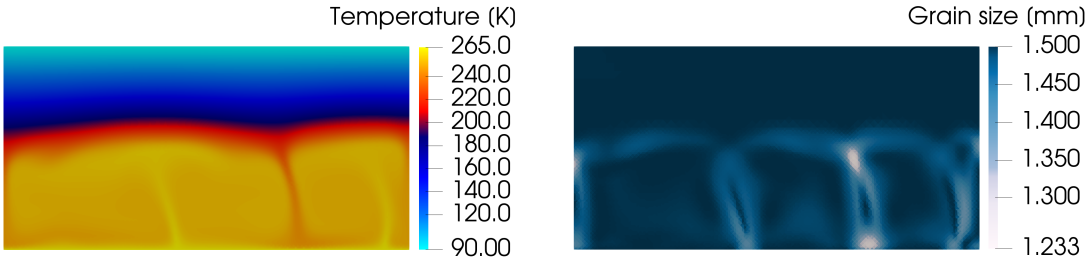

Figure 5.3: Case 4b), 96 Myr

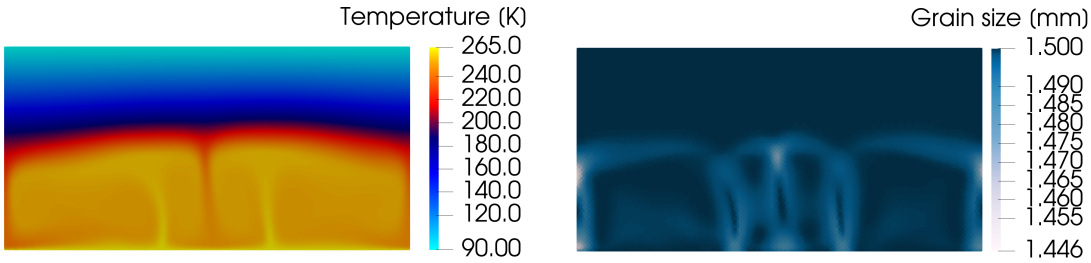

Figure 5.4: Case 4c), 50 Myr

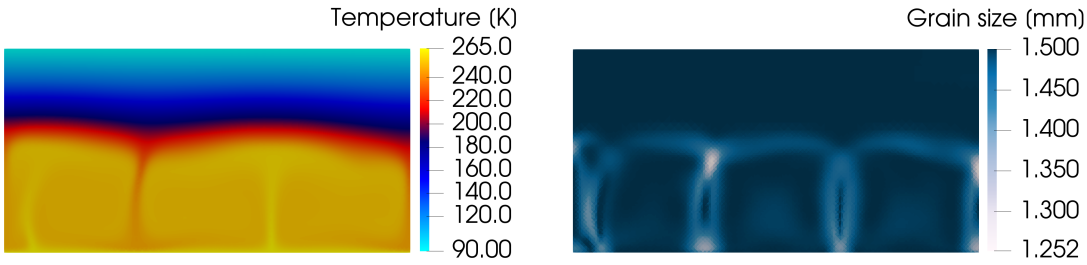

Figure 5.5: Case 4d), 85 Myr

The choice of parameters does not strongly affect the behaviour of the convention. We observe the creation of two convective cells for each case. Furthermore, the choice between the lab and ice core data does not affect the size of the grains, because the variations of the grain size for the same λ are nearly identical. On the other hand, the choice of λ does influence the range of the grain size, as we observe, that for Case 4b) the grain size varies from 1.233 mm to 1.5 mm and for Case 4d) the grain size varies from 1.252 mm to 1.5 mm. For Cases 4a) and 4c), the grain size attains the values from 1.462 mm to 1.5 mm and from 1.446 mm to 1.5 mm, respectively. We therefore deduce that the higher values of λ help reduce the grain size faster while the lower values tend to slow down the grain size reduction.

To conclude, all simulations show again the creation of two convective cells. In the snapshots illustrating the grain size, we can observe that the grain size is notably reduced on the boundary of each convective cell, to a small extent inside the cell and around each ascending and descending current of ice. The smallest grains occur on the upper boundary of the convecting part where the two cells meet.

The phenomenon of grain size reduction around the ascending currents is primarily driven by the high magnitude of the velocity gradient, which results in increased stress in these areas, thereby reducing the grain size. Similarly, around the descending currents, the grain size reduction is influenced by the high velocity gradient that creates higher stress, accelerating the reduction process and also by lower temperatures that inhibit the grain growth. This interplay of factors leads to the smallest grains being found within these regions. Additionally, small grain sizes can be observed on the upper boundaries of the convective cells, where higher temperatures and slightly increased stress are present compared to the non-convective parts or the cell interiors. Examination of convection patterns indicates that areas with smaller grain sizes correspond to regions with higher stress, typically found at the boundaries and around the ascending and descending currents. The smallest grain sizes are observed at the upper interface between two neighbouring convective cells, a result of the combination of lower temperatures and higher stress.

The behaviour of the convection in each case is very similar to the simulation in Case 2b) (Figure 4.2) with the constant grain size 1.42 mm. We can also observe that the grain reaches the size $d_{\max}$ almost everywhere. This underlines the significant role of the choice of the grain size limit $d_{\max}$. Moreover, we can assume that the grains would further increase their size because, for the temperature 265 K, the grain can grow at the order of 0.05 mm/year. Therefore, the grains, without imposing the upper limit on this size, would further grow to the point

when it would start to dampen the convection in the icy shell.

Furthermore, the grain size changes very rapidly with respect to the flow speed. This finding is based on (i) the evaluation of the grain growth rate from the previous paragraph and (ii) on the observation that despite the quick changes in the shape of the convective cells, the regions with smaller grain size copy the boundaries of the convective cells and also the ascending and descending currents. This suggests that since the grain size advection has only a minor effect, the equilibrium grain size can be computed directly on the mesh in every time step without solving the advection.

Conclusion

In this study, we developed a numerical model to explore the effects of the grain size on thermal convection within the ice layers of icy moons. The finite-element method was employed to solve the governing equations, incorporating temperature and stress-dependent material properties and dynamically evolving grain size.

Our simulations with the constant grain size demonstrate that the grain size plays a pivotal role in determining the convection regime within the ice layers. The results indicate that smaller grain sizes enhance convective activity, leading to chaotic convection for grains 0.45 mm large. For the grains 1.42 mm large, we observe the formation of multiple convective cells and decreased heat transfer, as evidenced by the higher Nusselt number. In contrast, for the grain size 4.48 mm, the system is fully in a conductive regime.

Finally, we implemented into our model of the thermal convection the grain size evolution [Behn et al., 2021]. The advection of the ice grains was performed by the Lagrangian tracer method [Kihoulou, 2024]. By including the grain size evolution model, the grain can reduce its size to 1.233 mm from 1.5 mm at points where the descending currents of the neighbouring cells meet. We then observe that grain size reduces its size around the ascending and descending currents inside each convective cell, while elsewhere, the grain size acquires its maximum threshold. Our study also demonstrates the great importance of the maximum grain size threshold in the icy shells of the moons since the majority of ice particles attain this value. Therefore, future research should focus on discovering this threshold to determine the behaviour of icy shells of the outer Solar System satellites.

Bibliography

M. Alnæs, J. Blechta, J. Hake, A. Johansson, B. Kehlet, A. Logg, C. Richardson, J. Ring, M. E. Rognes, and G. N. Wells. The FEniCS Project Version 1.5. *Archive of Numerical Software*, 3(100):9–23, 2015. doi: https://doi.org/10.11588/ans.2015.100.20553. URL https://doi.org/10.11588/ans.2015.100.20553.

A. C. Barr and W. B. McKinnon. Convection in ice I shells and mantles with self-consistent grain size. *Journal of Geophysical Research: Planets*, 112(E2), FEB 27 2007. ISSN 2169-9097. doi: 10.1029/2006JE002781. URL https://doi.org/10.1029/2006JE002781.

M. D. Behn, D. L. Goldsby, and G. Hirth. The role of grain size evolution in the rheology of ice: implications for reconciling laboratory creep data and the Glen flow law. *The Cryosphere*, 15(9):4589–4605, 2021. doi: 10.5194/tc-15-4589-2021. URL https://tc.copernicus.org/articles/15/4589/2021/.

B. Blankenbach, F. Busse, U. Christensen, L. Cserepes, D. Gunkel, U. Hansen, H. Harder, G. Jarvis, M. Koch, G. Marquart, D. Moore, P. Olson, H. Schmeling, and T. Schnaubelt. A Benchmark Comparison for Mantle Convection Codes. *Geophysical Journal International*, 98(1):23–38, Jul 1989. ISSN 0956-540X. doi: 10.1111/j.1365-246X.1989.tb05511.x. URL https://doi.org/10.1111/j.1365-246X.1989.tb05511.x.

E. Carnahan, N. S. Wolfenbarger, J. S. Jordan, and M. A. Hesse. New insights into temperature-dependent ice properties and their effect on ice shell convection for icy ocean worlds. *Earth and Planetary Science Letters*, 563:116886, 2021. URL https://doi.org/10.1016/j.epsl.2021.116886.

C. S. Cockell, T. Bush, C. Bryce, S. Direito, M. Fox-Powell, J. P. Harrison, H. Lammer, H. Landenmark, J. Martin-Torres, N. Nicholson, L. Noack, J. O'Malley-James, S. J. Payler, A. Rushby, T. Samuels, P. Schwendner, J. Wadsworth, and M. P. Zorzano. Habitability: A Review. *Astrobiology*, 16(1):89–117, JAN 1 2016. ISSN 1531-1074. doi: 10.1089/ast.2015.1295. URL https://doi.org/10.1089/ast.2015.1295.

W. B. Durham and L. A. Stern. Rheological Properties of Water Ice—Applications to Satellites of the Outer Planets. *Annual Review of Earth and Planetary Sciences*, 29:295–330, 2001. URL https://doi.org/10.1146/annurev.earth.29.1.295.

A. I. Ermakov, R. R. Fu, J. C. Castillo-Rogez, C. A. Raymond, R. S. Park, F. Preusker, C. T. Russell, D. E. Smith, and M. T. Zuber. Constraints on Ceres' Internal Structure and Evolution From Its Shape and Gravity Measured by the Dawn Spacecraft. *Journal of Geophysical Research: Planets*, 122(11):2267–2293, NOV 2017. ISSN 2169-9097. doi: 10.1002/2017JE005302. URL https://doi.org/10.1002/2017JE005302.

R. Feistel and W. Wagner. A New Equation of State for H2O Ice Ih. *Journal of Physical and Chemical Reference Data*, 35(2):1021–1047, 2006. URL https://doi.org/10.1063/1.2183324.

P. Fullsack. An arbitrary Lagrangian-Eulerian Formulation for Creeping Flows and its Application in Tectonic Models. *Geophysical Journal International*, 120 (1):1–23, JAN 1995. ISSN 0956-540X. doi: 10.1111/j.1365-246X.1995.tb05908.x. URL https://doi.org/10.1111/j.1365-246X.1995.tb05908.x.

D. L. Goldsby and D. L. Kohlstedt. Superplastic deformation of ice: Experimental observations. *Journal of Geophysical Research-Planets-Solid Earth*, 106(B6): 11017–11030, JUN 10 2001. ISSN 2169-9313. doi: 10.1029/2000JB900336. URL https://doi.org/10.1029/2000JB900336.

O. Grasset, M. K. Dougherty, A. Coustenis, E. J. Bunce, C. Erd, D. Titov, M. Blanc, A. Coates, P. Drossart, L. N. Fletcher, H. Hussmann, R. Jaumann, N. Krupp, J. P. Lebreton, O. Prieto-Ballesteros, P. Tortora, F. Tosi, and T. Van Hoolst. JUpiter ICy moons Explorer (JUICE): An ESA mission to orbit Ganymede and to characterise the Jupiter system. *Planetary and Space Science*, 78:1–21, APR 2013. ISSN 0032-0633. doi: 10.1016/j.pss.2012.12.002. URL https://doi.org/10.1016/j.pss.2012.12.002.

C. J. Hansen, J. Castillo-Rogez, W. Grundy, J. D. Hofgartner, E. S. Martin, K. Mitchell, F. Nimmo, T. A. Nordheim, C. Paty, L. C. Quick, J. H. Roberts, K. Runyon, P. Schenk, A. Stern, and O. Umurhan. Triton: Fascinating Moon, Likely Ocean World, Compelling Destination! *Planetary Science Journal*, 2 (4), AUG 2021. doi: 10.3847/PSJ/abffd2. URL https://doi.org/10.3847/PSJ/abffd2.

S. M. Howell and R. T. Pappalardo. NASA's Europa Clipper-a mission to a potentially habitable ocean world. *Nature Communications*, 11(1), MAR 11 2020. ISSN 2041-1723. doi: 10.1038/s41467-020-15160-9. URL https://doi.org/10.1038/s41467-020-15160-9.

B. Journaux, T. Chauve, M. Montagnat, A. Tommasi, F. Barou, D. Mainprice, and L. Gest. Recrystallization processes, microstructure and crystallographic preferred orientation evolution in polycrystalline ice during high-temperature simple shear. *Cryosphere*, 13(5):1495–1511, MAY 27 2019. ISSN 1994-0416. doi: 10.5194/tc-13-1495-2019. URL https://doi.org/10.5194/tc-13-1495-2019.

M. Kihoulou. *User manual to the MillFEuiIle code*. Department of Geophysics, Faculty of Mathematics and Physics, Charles University, 2024. Available at https://geo.mff.cuni.cz/~kihoulou/mf/MilleFEuiIle_manual.pdf.

M. Kihoulou, O. Cadek, J. Kvorka, K. Kalousova, G. Choblet, and G. Tobie. Topographic response to ocean heat flux anomaly on the icy moons of Jupiter and Saturn. *Icarus*, 391, FEB 2023. ISSN 0019-1035. doi: 10.1016/j.icarus.2022.115337. URL https://doi.org/10.1016/j.icarus.2022.115337.

S. Linow, M. W. Hörhold, and J. Freitag. Grain-size evolution of polar firn: a new empirical grain growth parameterization based on X-ray microcomputer tomography measurements. *Journal of Glaciology*, 58(212):1245–1252, 2012. doi: 10.3189/2012JoG11J256. URL https://doi.org/10.3189/2012JoG11J256.

A. Logg, K.-A. Mardal, and G. Wells, editors. *Automated Solution of Differential Equations by the Finite Element Method*, volume 84. Springer-Verlag Berlin Heidelberg, 2012. doi: http://dx.doi.org/10.1007/978-3-642-23099-8. URL https://doi.org/10.1007/978-3-642-23099-8.

R. D. Lorenz, E. P. Turtle, J. W. Barnes, M. G. Trainer, D. S. Adams, K. E. Hibbard, C. Z. Sheldon, K. Zacny, P. N. Peplowski, D. J. Lawrence, M. A. Ravine, T. G. McGee, K. S. Sotzen, S. M. MacKenzie, J. W. Langelaan, S. Schmitz, L. S. Wolfarth, and P. D. Bedini. Dragonfly: A rotorcraft lander concept for scientific exploration at titan. *Johns Hopkins APL Technical Digest*, 34(3): 374–387, OCT 2018. ISSN 0270-5214.

T. B. McCord and C. Sotin. Ceres: Evolution and current state. *Journal of Geophysical Research: Planets*, 110(E5), 2005. doi: https://doi.org/10.1029/2004JE002244. URL https://doi.org/10.1029/2004JE002244.

F. Nimmo and R. T. Pappalardo. Ocean worlds in the outer solar system. *Journal of Geophysical Research-Planets*, 121(8):1378–1399, AUG 2016. ISSN 2169-9097. doi: 10.1002/2016JE005081. URL https://doi.org/10.1002/2016JE005081.

F. Nimmo, D. P. Hamilton, W. B. . McKinnon, P. M. Schenk, R. P. Binzel, C. J. Bierson, R. A. Beyer, J. M. Moore, S. A. Stern, H. A. Weaver, C. B. Olkin, L. A. Young, K. E. Smith, and New Horizons Geology Geophys. Reorientation of Sputnik Planitia implies a subsurface ocean on Pluto. *Nature*, 540(7631): 94+, DEC 1 2016. ISSN 0028-0836. doi: 10.1038/nature20148. URL https://doi.org/10.1038/nature20148.

E. Picard. Mémoire sur la théorie des équations aux dérivées partielles et la méthode des approximations successives. *Journal de Mathématiques Pures et Appliquées*, 6:145–210, 1890. URL http://eudml.org/doc/235808.

K. Röttger, A. Endriss, J. Ihringer, S. Doyle, and W. F. Kuhs. Lattice constants and thermal expansion of H2O and D2O ice Ih between 10 and 265 K. *Acta Crystallographica Section B: Structural Science*, 50(6):644–648, 1994. URL https://doi.org/10.1107/S010876819400493X.

C. Sotin, K. Kalousová, and G. Tobie. Titan's Interior Structure and Dynamics After the Cassini-Huygens Mission. *Annual Review of Earth and Planetary Sciences*, 49(Volume 49, 2021):579–607, 2021. ISSN 1545-4495. doi: https://doi.org/10.1146/annurev-earth-072920-052847. URL https://www.annualreviews.org/content/journals/10.1146/annurev-earth-072920-052847.

C. Taylor and P. Hood. A numerical solution of the Navier-Stokes equations using the finite element technique. *Computers and Fluids*, 1(1):73 – 100,

1973. doi: 10.1016/0045-7930(73)90027-3. URL https://doi.org/10.1016/0045-7930(73)90027-3.

Q. Wang, S. Fan, and C. Qi. Grain growth of ice doped with soluble impurities. *Cryosphere*, 18(3):1053–1084, MAR 5 2024. ISSN 1994-0416. doi: 10.5194/tc-18-1053-2024. URL https://doi.org/10.5194/tc-18-1053-2024.

List of Figures

List of Tables